

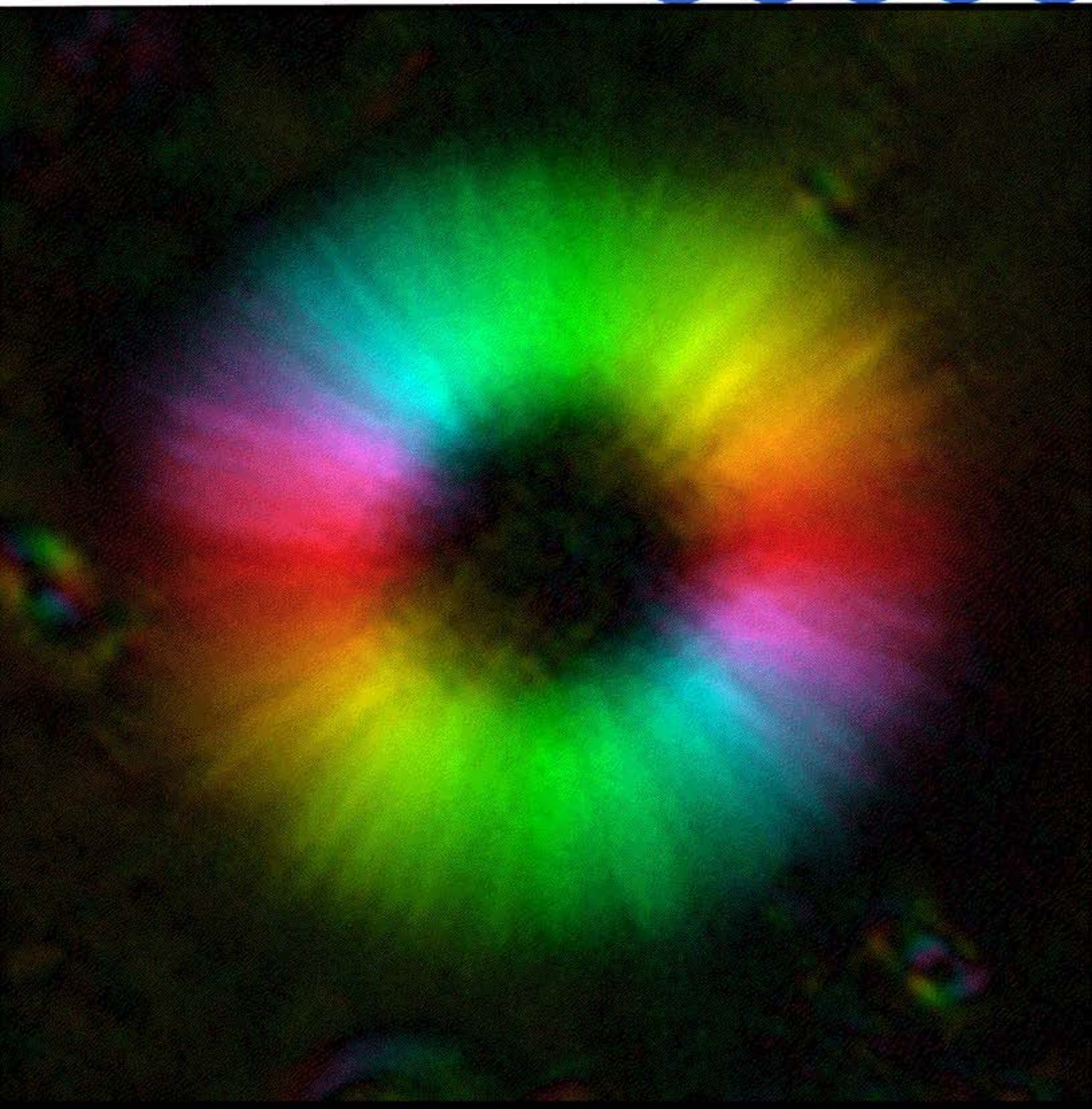
Journal of

ISSN 0022-2720 CODEN JMICAR

Microscopy

Blackwell Science

Volume 180, Part 2, November 1995



The Journal is published monthly and the subscription price for 1995 for four volumes comprising 12 parts in total is £376.00 (Europe), \$642.00 (U.S.A. and Canada), £414.00 (elsewhere). Subscribers in Canada must add 7% to the subscription price, to allow for GST. Subscribers in Europe must quote their VAT registration number or state that they are not registered. Subscribers in the Netherlands who are not VAT registered must add 6% to the subscription price, to allow for VAT. Outside Europe, the journal is despatched by various forms of airspeeded delivery. Second-class postage paid at Rahway, NJ. Postmaster, send address corrections to *Journal of Microscopy*, c/o Mercury Airfreight International Inc., 2323 Randolph Avenue, Avenel, NJ 07001, U.S.A. Current issues for the Indian subcontinent, Australasia and the Far East are sent by air to regional distribution points from where they are forwarded to subscribers by surface mail. Any back numbers are normally despatched by surface to all regions, except North America, where they are sent by a.s.p., and India, where they are sent by air freight. Subscription orders and all correspondence relating to subscriptions and back issues should be addressed to Journal Subscriptions, Blackwell Science Ltd, PO Box 88, Oxford OX2 0NE. Tel. (+44) 1865 20 206, Fax (+44) 1865 206219.

This journal is included in the ADONIS system, whereby copies of individual articles can be printed out from compact discs (CD-ROM) on demand. An explanatory leaflet giving further details of the scheme is available from the publishers on request.

The publisher's policy is to use acid-free permanent paper, to the draft standard ISO/DIS/9706, made from sustainable forests using chlorine-free pulp. The paper used in this journal has an ECO-CHECK 4 star rating.

FRONT COVER

Single aster consisting of microtubules radiating in all directions from the centrosome, a microtubule organizing centre found in almost all animal cells. False-colour version of the black and white image shown in the centre of Fig. 3, p. 143, by Oldenbourg & Mei. The hue represents the azimuth of the slow axis direction of the measured retardance in each pixel.

Volume 180 Part 2 November 1995

Marine Biological Laboratory/
Woods Hole Oceanographic Institution
Woods Hole, MA 02543

Contents

DEC 1 1995

- J. HONGPAISAN AND G. M. ROOMANS. Use of *post mortem* and *in vitro* tissue specimens for X-ray microanalysis, 93
- O. S. HEAVENS. Use of the approximations in cell studies by total internal reflection fluorescence microscopy (TIRF), 106
- K. D. NISWENDER, S. M. BLACKMAN, L. ROHDE, M. A. MAGNUSON AND D. W. PISTON. Quantitative imaging of green fluorescent protein in cultured cells: comparison of microscopic techniques, use in fusion proteins and detection limits, 109
- D. A. ORLOVICH AND A. E. ASHFORD. X-ray microanalysis of ion distribution in frozen salt/dextran droplets after freeze-substitution and embedding in anhydrous conditions, 117
- R. H. NEWTON, J. P. HAFEGEE AND M. W. HO. Polarized light microscopy of weakly birefringent biological specimens, 127
- L. S. CUTTS, P. A. ROBERTS, J. ADLER, M. C. DAVIES AND C. D. MELIA. Determination of localized diffusion coefficients in gels using confocal scanning laser microscopy, 131
- R. OLDENBOURG AND G. MEI. New polarized light microscope with precision universal compensator, 140
- A. ENTWISTLE. The effects of total internal reflection on the spread function along the axis in confocal microscopy, 148
- L. FRANK AND F. MATĚJKA. Edge effect in Auger electron microscopy: quantification of the effect, 158
- K. PROPSTRA AND N. E. VAN HULST. Polarization contrast in photon scanning tunnelling microscopy combined with atomic force microscopy, 165
- G. R. BUSHELL, G. S. WATSON, S. A. HOLT AND S. MYHRA. Imaging and nano-dissection of tobacco mosaic virus by atomic force microscopy, 174
- Short technical notes**
- D. A. HOWELL, J. W. HECKMAN JR AND M. A. CRIMP. Preparation of metal multilayer TEM cross-sections using ultramicrotomy, 182
- Z. SHAO AND A. P. SOMLYÓ. Stereo representation of atomic force micrographs: optimizing the view, 186

continued overleaf

b
Blackwell
Science



0022-2720(199511)180:2:1-I

New polarized light microscope with precision universal compensator

R. OLDENBOURG & G. MEI

Marine Biological Laboratory, Woods Hole, MA 02543, U.S.A.

Key words. Polarimetry, birefringence, modulator, liquid crystal.

Summary

A new type of polarized light microscope ('new pol-scope') for fast and orientation-independent measurement of birefringent fine structure has been developed. The design of the new pol-scope incorporates a precision universal compensator made from two liquid crystal variable retarders. A video camera and digital image processing system provide fast measurements of specimen anisotropy (retardance magnitude and azimuth) at all points of the image forming the field of view. The images document fine structural and molecular organization within a thin optical section of the specimen. The sensitivity of the current instrument is 0.1 nm of specimen retardance, measured with data gathered in 0.43 s at all 640×480 image points. Examples of birefringence measurements in biological (microtubule arrays) and industrial (magneto-optical disc substrate) specimens are presented.

1. Introduction

Based on its great analytical power, the polarized light microscope has found numerous applications in fields such as biology, mineralogy, metallography, chemistry and for forensic studies (Chamot & Mason, 1958; Hartshorne & Stuart, 1960; Inoué, 1986; McCrone, 1991). In biology, the polarized light microscope has the unique potential to measure submicroscopic molecular organization dynamically and non-destructively in samples that, in general, can be kept in native environmental conditions. With the traditional polarized light microscope, however, single images display only those anisotropic structures that have a limited range of orientations with respect to the polarization axes of the microscope. Furthermore, rapid measurements are restricted to a single image point or single area that exhibits uniform birefringence or other form of optical anisotropy (Allen *et al.*, 1963), while measurements comparing several image points take an inordinately long time (Inoué & Sato, 1966).

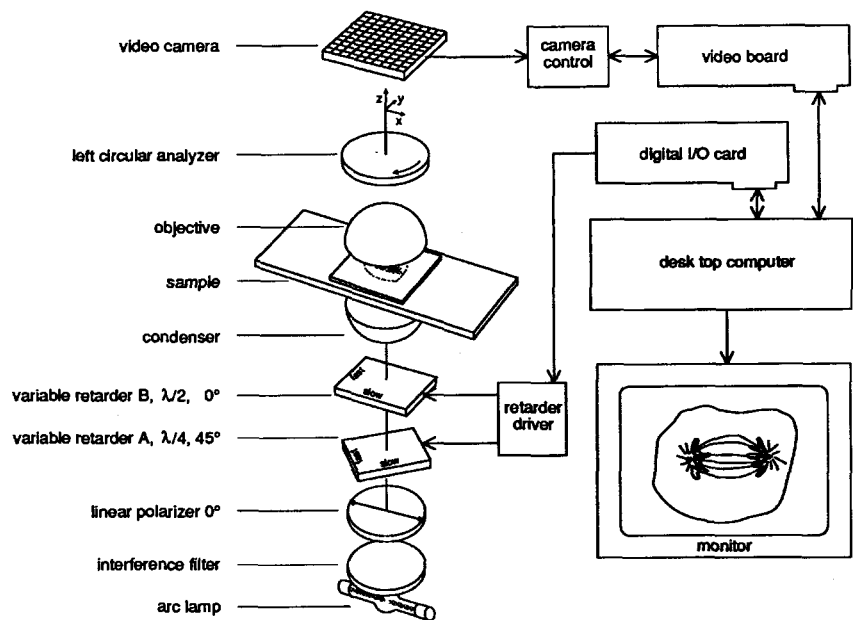
To overcome the limitations of the traditional polarized

light microscope, we have developed a new type of polarized light microscope ('new pol-scope'), which incorporates a precision universal compensator made of two liquid crystal variable retarders. The two variable retarders are computer controlled and replace the traditional compensator of the polarizing microscope. The new microscope optical set-up, plus a video camera and a specially designed, computerized image analysis system provide fast measurements of specimen anisotropy (retardance magnitude and azimuth) at all points of the image constituting the field of view, irrespective of birefringence axes. Because of its fast speed, high sensitivity and ease of use for measurements of optical anisotropies, the new instrument significantly advances the analytical power of the polarizing microscope in all its traditional application areas.

We note that the proposed measurement scheme is not limited to polarizing microscopy and it can be used in other imaging or non-imaging applications involving precision polarimetry. Therefore, we expect applications of the proposed measurement scheme to evolve in other areas, including ellipsometry, remote sensing, material science, and manufacturing and processing control of plastic and glass materials.

This article reports the first complete description of design and implementation of the instrument to measure linear retardances (birefringence) in a transparent microscopic specimen (parts of the design concept and implementation were previously reported by us in a proceedings article; Mei & Oldenbourg, 1994; and in US patent application Serial No. 08/241, 842). We first present the design outline including the polarization optical concept of the universal compensator. Next, we discuss a specific algorithm to measure small specimen retardances at high spatial and temporal resolution concurrently for the whole field of view. This algorithm is then extended to include a background correction procedure which corrects for polarization aberrations introduced by different components in the optical train, such as high-numerical-aperture (NA) lenses. With the background correction procedure the measurement set-up is able to measure reliably specimen

Fig. 1. Schematic of the new polarized light microscope. The optical design (left part) builds on the traditional polarized light microscope with the conventional compensator replaced by two liquid crystal variable retarders A and B forming the precision universal compensator. Retarder A is set at a quarter wave retardance and is orientated with its slow axis at 45° with respect to the linear polarizer. The combination of polarizer and retarder A produces left circularly polarized light. Retarder B, set at a half wave retardance, flips the polarization to right circularly polarized. The right circularly polarized light is effectively blocked by the left circular analyser. Retardances A and B are varied by varying the voltages applied to the liquid crystal devices using the retarder drivers. Any given retardance from the specimen or other elements in the optical train are compensated by adjusting retardances A and B without mechanically rotating any of the optical components (see text). The video camera and electronic parts shown on the right of the figure provide for image recording and analysis and for instrument control.



retardance values below 0.1 nm in magnitude. In the last section we describe the instrumentation and procedures currently used to implement the new pol-scope.

2. Design outline

The design of the new pol-scope builds on the traditional polarized light microscope introducing two essential modifications: the specimen is illuminated with nearly circularly polarized light and the traditional compensator is replaced by two electro-optical modulators (Fig. 1). The two electro-optical modulators are currently implemented as liquid crystal devices that function as linear retarders whose retardance values are varied independently by a voltage applied to each device. As indicated in Fig. 1, the slow axes of the linear retarders are mutually orientated at 45° . By adjusting the liquid crystal retardances, this combination of variable retarders can compensate any specimen retardance, regardless of orientation and magnitude, so that a minimum of light equal to extinction passes through the analyser. The two variable retarders thus act together as a universal compensator.

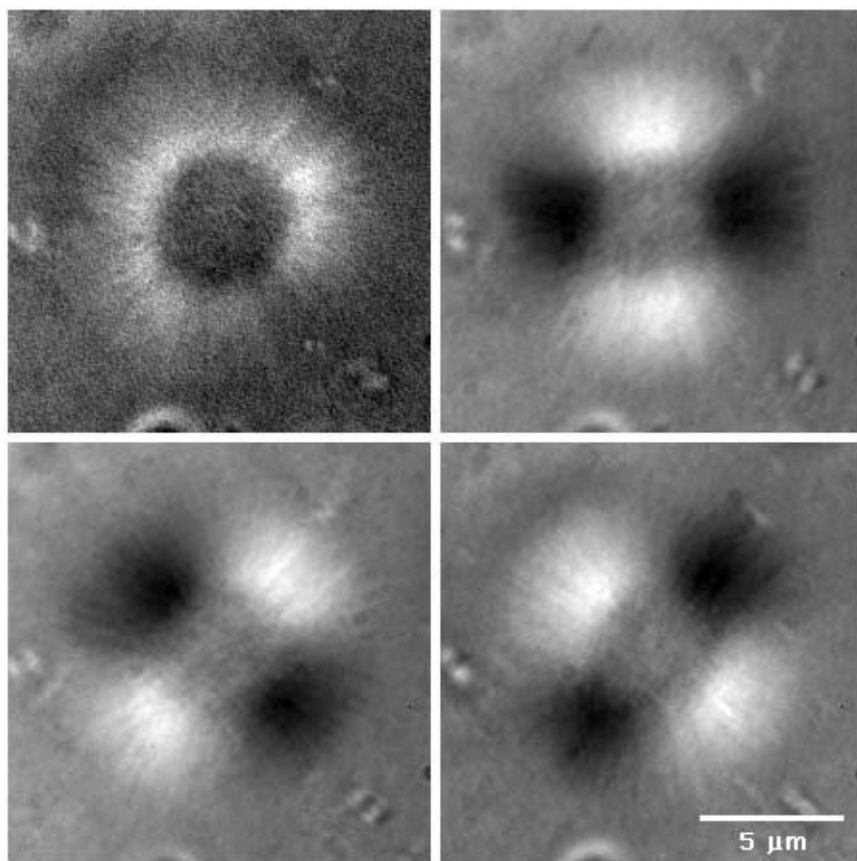
To illustrate the workings of the universal compensator, we show four different images (Fig. 2) of the same specimen, a so-called aster formed in lysate prepared from eggs of the surf clam (Oldenbourg *et al.*, 1993). Asters are convenient test objects because their radial symmetric structure contains astral rays orientated in all directions, with each ray possessing a linear retardance of a fraction of one nanometre to several nanometres and a slow axis orientated parallel to the ray axis (astral rays are bundles

of microtubule polymers that are formed at the poles of the mitotic spindle in dividing animal cells). The images in Fig. 2 were recorded with the set-up illustrated in Fig. 1 and described in more detail in the Instrumentation section. In the top left image of Fig. 2 the specimen is illuminated with right circularly polarized light. Astral rays appear bright, regardless of their orientation, against the dark background. Background light is effectively blocked by the left circular analyser. In the top right image of Fig. 2, the specimen is illuminated with elliptically polarized light and astral rays orientated at 45° to the principal axes of the polarization ellipse appear either brighter (vertical microtubules) or darker (horizontal microtubules) than the background. The horizontal/vertical position of dark and bright quadrants of the aster in the top right image of Fig. 2 corresponds to the horizontal/vertical orientation of the slow/fast axis of linear retarder B. On the other hand, the diagonal position of dark and bright quadrants of the aster in the bottom two images of Fig. 2 corresponds to the diagonal orientation of the slow/fast axis of retarder A.

We want to emphasize here that during recordings of all four images in Fig. 2, no part of the microscope set-up, including the specimen, was mechanically rotated. To obtain the four images, only the voltages applied to the liquid crystals were changed. Therefore, all four images recorded with the CCD camera are in perfect register, with corresponding picture elements representing intensities of the same object element. Experimental and theoretical results obtained by Hansen *et al.* (1988) indicate that the diffraction anomaly reported for polarizing microscope systems using linearly polarized light (Inoué & Kubota,

$$A = \lambda/4, B = \lambda/2$$

$$A = \lambda/4, B = (\lambda/2) - 16 \text{ nm}$$



$$A = (\lambda/4) - 16 \text{ nm}, B = \lambda/2$$

$$A = (\lambda/4) + 16 \text{ nm}, B = \lambda/2$$

Fig. 2. CCD-camera recorded images of a single aster consisting of microtubules radiating in all directions from the centrosome, a microtubule organizing centre. Images of the aster were recorded using four different settings of retarders A and B with retardance settings indicated above and below the images. λ is 546 nm, the wavelength of the illuminating light. (Images are contrast enhanced for better printing.)

1958) is substantially reduced in microscopes which use nearly circularly polarized light, as is the case in the new pol-scope. Optimal image registration and absence of diffraction anomaly is particularly important for measurements requiring high spatial resolution.

The retarder settings for images in Fig. 2 compensate the retardance of astral rays orientated either horizontally (top right image) or diagonally (bottom two images). We found that astral rays of any other orientation can also be compensated with retarder settings A and B that in general will both deviate from their extinction settings of a quarter wave (A) and half wave (B). In fact, we have found an expression that relates the retarder settings A and B to the specific specimen retardance that these retarder settings compensate. In the following formulae the magnitude of specimen retardance is given as R , typically in nanometres, and its slow axis orientation is Θ . Θ is measured in degrees in the x - y plane starting from the positive x -axis (refer to coordinate axes specified in Fig. 1). The retarder settings A and B that compensate the specimen retardance are given in terms of α_{\min} and β_{\min} with $A = (\lambda/4) + \alpha_{\min}$ and

$B = (\lambda/2) + \beta_{\min}$ (the subscript min indicates that for these retarder settings a minimum intensity equal to extinction is recorded for the given specimen retardance characterized by R and Θ):

$$R = \sqrt{\alpha_{\min}^2 + \beta_{\min}^2}, \quad (1)$$

$$\Theta = 90^\circ - \text{Sign}(\alpha_{\min}) 45^\circ + \frac{\arctan\left(\frac{\beta_{\min}}{\alpha_{\min}}\right)}{2}. \quad (2)$$

The $\text{Sign}(\alpha_{\min})$ function is either +1 for positive α_{\min} or -1 for negative α_{\min} .

Equations (1) and (2) were first found by modelling the optical set-up with a computer program written in Mathematica (Wolfram Research Inc., Champaign, IL). The program simulates a single ray that first passes through the linear polarizer, then the two variable retarders, then the specimen and finally the circular analyser. The computer simulation was based on the Stokes-formalism to describe the polarization state of the light ray. The polarization-sensitive devices were represented by their corresponding Mueller-matrices to predict the new polarization state after the ray passed through the

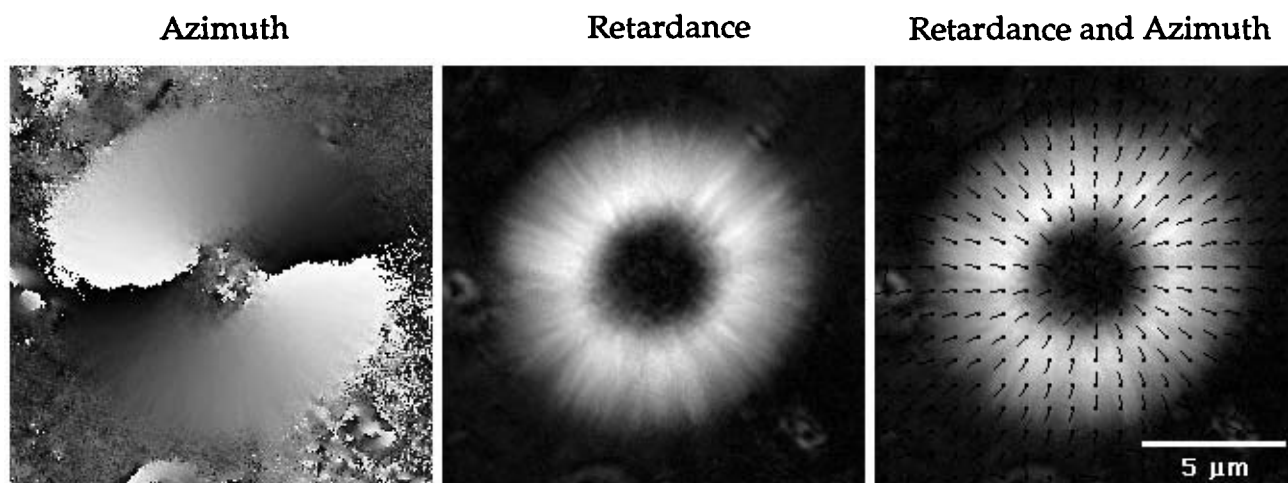


Fig. 3. Images computed from raw image data shown in Fig. 2. In the Retardance image in the top centre, white corresponds to a maximum retardance magnitude of 3.9 nm, black corresponds to zero retardance, with greys indicating retardance values in between. In the Azimuth image on the top left, black indicates zero azimuth, i.e. slow axis of measured retardance orientated horizontally, medium grey indicates azimuth 90°, i.e. slow axis vertical, and white indicates an azimuth of 180°, which corresponds again to a horizontal slow axis. Other grey values indicate azimuth angles between 0° and 180°. In the right image, both Retardance and Azimuth are given, with the azimuth indicated by lines with orientations between 0° and 180°. To reduce the complexity of this image we chose to display the azimuth on regular grid points (indicated by small closed circles) at a much lower resolution than the original measurements permits.

device. The effect of several linked devices can be computed by multiplying the corresponding matrices in the right order (see e.g. Shurcliff, 1962; Kliger *et al.*, 1990). A more detailed description of the mathematical foundations of the algorithms used with the new pol-scope will be published separately.

Using the computer simulation we found that a given specimen retardance of any magnitude and azimuth can be compensated with the two variable retarders, so that a minimum intensity equal to extinction is recorded with particular retarder settings. Equations (1) and (2), however, only apply if the specimen retardance is small. For a specimen retardance equal to $\lambda/20$, with λ the wavelength of light used in the measurement, the systematic error introduced by using Eqs. (1) and (2) to compute the specimen retardance from the measured $(\alpha_{\min}, \beta_{\min})$ is about 2%. With a specimen retardance of $\lambda/40$ the error in the computed magnitude and azimuth reduces to about 0.5%. In fact, for measuring small birefringence values, we have identified a very efficient measurement process and computational algorithm, which we discuss next.

3. Theory of measuring small, linear retardances ($< \lambda/20$)

The four images shown in Fig. 2 are indeed sufficient to compute the specimen retardance and orientation of the slow axis (azimuth) in every image point. In other words, the retardance of every astral ray, regardless of its orientation, can be computed using simple image arithmetic

involving the four images of Fig. 2. By way of explanation, we consider the intensities I_1 to I_4 recorded in a single, corresponding picture element (pixel) of the four images. Each of these four intensities depends on the compensator settings $A = (\lambda/4) + \alpha$ and $B = (\lambda/2) + \beta$ and on the retardance of the small specimen region that is imaged at this pixel. When the specimen retardance and the changes in compensator settings (α and β) are small in retardance magnitude ($< \lambda/20 \approx 25$ nm) the following quadratic expression holds:

$$I_n = I_0[(\alpha_n - \alpha_{\min})^2 + (\beta_n - \beta_{\min})^2] + I_{\min}, \quad (3)$$

with n from 1 to 4 for each pixel. (Eq. 3 is a quadratic approximation of the complete expression involving the square of trigonometric functions of retardances. The approximation introduces a systematic error which is less than 3% for retardances less than 25 nm.) In the first, top left image of Fig. 2, for example, α_1 and β_1 were both zero and the intensity I_1 is proportional to the square of the magnitude of specimen retardance R . I_0 is the proportionality factor and is equal to the intensity observed at total transmission. I_{\min} is the intensity observed when the specimen retardance is compensated by the variable retarder settings, i.e. when $\alpha_n = \alpha_{\min}$ and $\beta_n = \beta_{\min}$. I_{\min} is the intensity equal to extinction and can be non-zero due to imperfections in the optics, or due to multiple scattering in the specimen.

Images in Fig. 2 were recorded using four fixed retarder

settings:

$$(\alpha_1 = 0, \beta_1 = 0), \quad (4a)$$

$$(\alpha_2 = 0, \beta_2 = -X), \quad (4b)$$

$$(\alpha_3 = -X, \beta_3 = 0), \quad (4c)$$

$$(\alpha_4 = +X, \beta_4 = 0), \quad (4d)$$

with $X = 16$ nm retardance. Four independent settings are necessary because Eq. (3) has four unknown parameters ($I_0, I_{\min}, \alpha_{\min}, \beta_{\min}$) and three known parameters (I_n, α_n and β_n). With the particular settings chosen in Eq. (4), the four quadratic equations derived from Eq. (3) have simple solutions for the unknowns α_{\min} and β_{\min} :

$$\alpha_{\min} = \frac{I_4 - I_3}{4I_1 - 2I_3 - 2I_4} X, \quad (5)$$

$$\beta_{\min} = \frac{I_4 + I_3 - 2I_2}{4I_1 - 2I_3 - 2I_4} X. \quad (6)$$

Note that α_{\min} and β_{\min} are calculated independent of I_0 and I_{\min} . Therefore, these parameters do not need to be determined separately. To find the desired expression for the specimen retardance R and azimuth Θ in terms of the measured intensities I_1 to I_4 , we simply need to replace in Eqs. (1) and (2) the terms α_{\min} and β_{\min} with the right sides of Eqs. (5) and (6). In fact, the computation of specimen retardance can be done for the entire viewing field at once by implementing Eqs. (1) and (2) with (5) and (6) as two sequences of image arithmetic functions. The first sequence produces an image representing the magnitude of specimen retardance, the second sequence produces an image representing the azimuth (Fig. 3). The images can be displayed either separately or combined using some special coding scheme. Thus, displayed images represent a direct visualization of specimen retardance measured at the spatial resolution of the light microscope optics. Furthermore, since the computed specimen retardance is independent of I_0 and I_{\min} , the resultant images are corrected for shading introduced by inhomogeneous specimen illumination, and for unpolarized background light, which stems, for example, from non-ideal polarizers, or from excessive light scattering by turbid samples.

4. Background correction procedure

With the analysis outlined above the instrument is capable of measuring specimen retardances between approximately 0.5 and 25 nm. The upper limit is given by the approximations used in deriving Eqs. (1)–(3), while the lower limit is caused by polarized background light that stems from polarization aberrations introduced, in part, by the strong curvature of high-NA lens surfaces in the optical train (Inoué & Hyde, 1957; Chipman, 1989). Polarization aberrations originating from different parts in the microscope optical train are

projected into the specimen space and cause an apparent retardance ('background retardance') that varies slowly across the viewing field (Fig. 4). In Fig. 4 we show images recorded from a preparation of single mitrotubules in aqueous solution (Tran *et al.*, 1994). As can be seen, images of these weakly birefringent objects are seriously affected by background retardances. While the background azimuth generally can take on any angle (see Fig. 4), we found that with care in the selection of strain-free microscope optics, slide and cover glass, the magnitude of background retardance can be quite small and uniform over a significant area, in the range of 0–0.5 nm. Furthermore, we found that for a given pixel, the background retardance is nearly constant in time and can be subtracted from the specimen retardance using the following procedure.

First, four specimen images are taken of the kind shown in Fig. 2. Then, the specimen, which is sandwiched between microscope slide and cover glass, is moved sideways on the microscope stage until a clear area with no specimen birefringence is imaged. A second set of four images is recorded with the same voltage settings as used before. The second set of four images measure the background retardances. Next, the $\alpha_{\min BG}$ and $\beta_{\min BG}$ values of the background retardances are computed using Eqs. (5) and (6) and the intensities recorded in the background set of images. Similarly, with the first set of images, representing specimen plus background retardances, the $\alpha_{\min SP, BG}$ and $\beta_{\min SP, BG}$ values are computed. To compute the retardance magnitude and azimuth associated with the specimen only, α_{\min} and β_{\min} in Eqs. (1) and (2) are substituted with

$$\alpha_{\min SP} = \alpha_{\min SP, BG} - \alpha_{\min BG},$$

and

$$\beta_{\min SP} = \beta_{\min SP, BG} - \beta_{\min BG}.$$

The images shown in Fig. 4 demonstrate the effectiveness of this background correction procedure.

The above procedure can also be used to measure small changes in retardance over time or between different focus levels. Figure 5 documents the retardance of a magneto-optical disc substrate, which was measured by first focusing on the disc surface imaging the moulded pits and grooves on the disc surface. The subsequent background set of images was taken by focusing a few micrometres above the disc surface, completely blurring the surface features. The retardance images shown in Fig. 5 were then computed by using the in-focus set of images as specimen set and the out-of-focus set as background.

Figure 5 demonstrates the result of yet a different kind of background subtraction that is achieved using the liquid crystal retarders. The magneto-optical disc substrate possesses a uniform retardance of about 18 nm in magnitude (fast axis orientated radially from the disc centre) owing to the partial alignment of polymers during

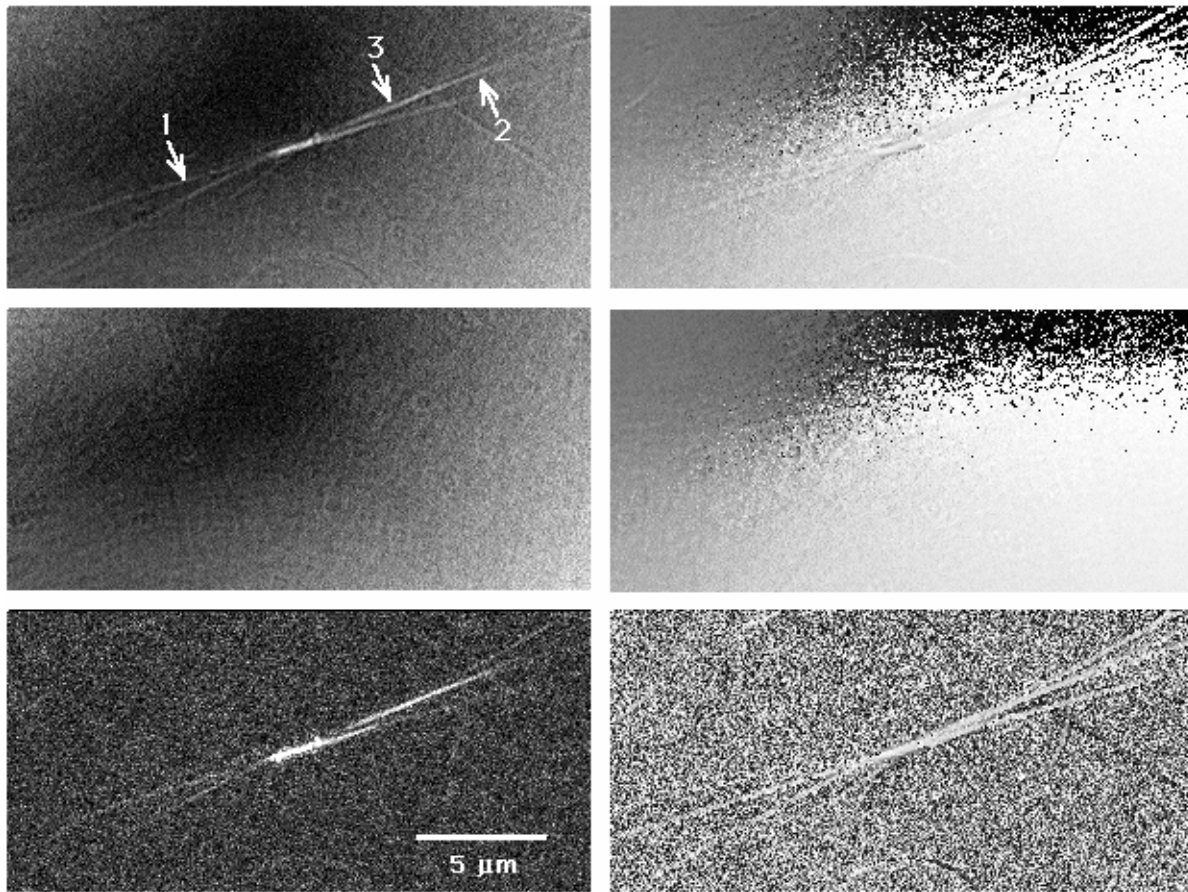


Fig. 4. Demonstration of background correction procedure on retardance and azimuth images of microtubules (single microtubules are 25 nm thick, several micrometres long, stiff and weakly birefringent biopolymers). In the sample imaged here microtubules grow off the ends of a short piece of axoneme, a birefringent rod-shaped polymerization seed (near image centre) which is stuck to the microscope coverglass. The specimen images in the top row (left: retardance image, right: azimuth image) are noticeably affected by background retardance. The centre row shows images of the background alone recorded after the preparation was moved sideways to view a clear specimen area. The bottom row shows the same specimen images as in the top row after the background correction procedure was applied (see text). The background-corrected specimen images show a uniform background with noise due to uncertainties in measured intensities (see text). The retardance of microtubule bundles, containing one or more microtubules growing off the ends of axonemes, was measured to be in the range of 0.07–0.21 nm. (Sample preparation and images by Phong T. Tran.)

the extrusion process. The uniform retardance is not visible in the images of Fig. 5 because it was optically compensated during the measurement by readjusting the liquid crystal retarder settings. Therefore, any retardance, due to grooves and pits for example, leading to deviations from the uniform background retardance was measured very sensitively.

The described optical method of compensating background retardance is most useful to subtract a uniform bias retardation in the sample or anywhere else in the optical train of the microscope. However, variations of background retardance within a given field of view cannot be compensated using the optical method, but these local retardance variations are corrected with the computational background correction procedure described earlier. The optical and computational methods of background correction are therefore complementary.

After background retardances are properly corrected for, the minimum specimen retardance that can be measured depends on the uncertainties of recorded image intensities. In Fig. 4 for example, the bottom images, which are background corrected, show random fluctuations in measured retardance due to uncertainties in measured image intensities. In CCD cameras, uncertainties in measured image intensities are due to several sources, such as photon statistics noise, CCD read-out noise and amplifier noise (in our measurements, light levels were high enough that photon statistics noise was negligible). In image parts with no specimen retardance, random intensity fluctuations result in an apparent retardance in each pixel that has a root-mean-square magnitude proportional to the standard deviation of the fluctuations and an azimuth angle that varies randomly between 0° and

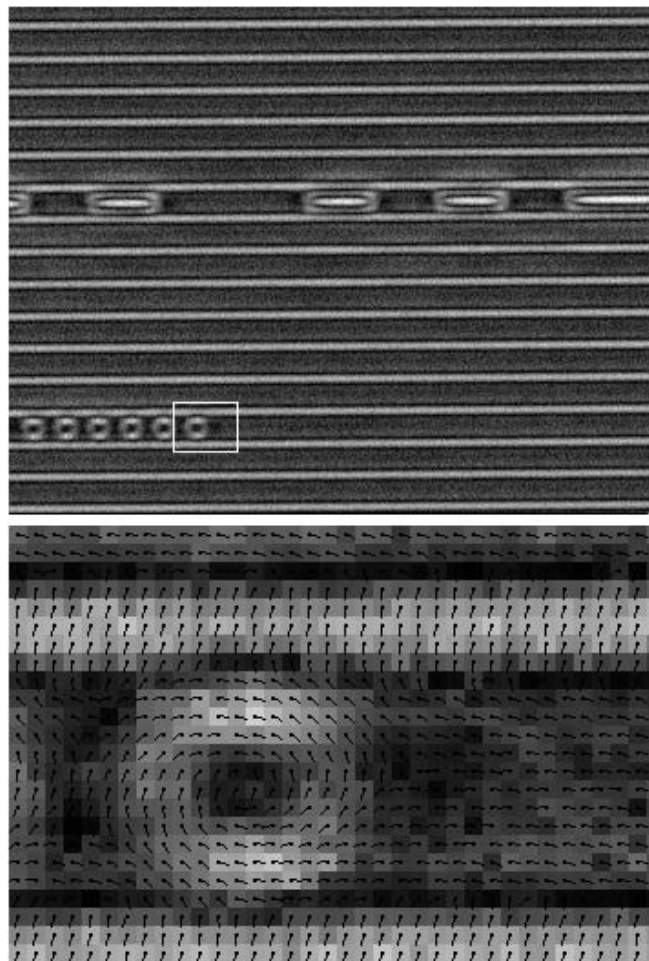


Fig. 5. Surface of magneto-optic disc substrate (polycarbonate) imaged with the new pol-scope. Top image: retardance magnitude near moulded pits and grooves (maximum retardance 5.6 nm, grooves are 1.3 μm apart). As explained in the text, the displayed retardances are the values measured as deviation from the uniform retardance (approximately 18 nm, slow axis parallel groove direction) of the polycarbonate bulk material. Lower image: small boxed area in top panel enlarged with measured azimuth orientations indicated for each pixel by short lines.

180°. With the instrumentation described in the next section we have achieved noise levels that correspond to 0.1 nm root-mean-square retardance per pixel with proportionately reduced noise when averaged over several pixels.

5. Instrumentation and procedures

The new pol-scope system illustrated in Fig. 1 was first implemented on an upright research grade microscope (Microphot-SA, Nikon Inc., Melville, NY; images in Figs. 2–5 were recorded using a 60 \times /1.4-NA Plan Apochromatic objective lens and 1.4-NA apochromatic condenser). For intense monochromatic light and homogeneous illumination we use a mercury arc lamp with Ellis light scrambler

(Technical Video, Woods Hole, MA) and narrow band pass interference filter (546 nm, 10 nm FWHM, Omega, Brattleboro, VT). Linear polarizer and left circular analyser (Meadowlark Optics, Longmont, CO) are inserted into the microscope optical path at the same places where they are located for traditional polarized light microscopy. The liquid crystal variable retarders (Cambridge Research and Instrumentation Inc. (CRI), Cambridge, MA) are placed in custom-made rotatable mounts on top of the field lens near the base of the microscope stand. The magnitude of retardance of the liquid crystal devices is adjusted with an AC square wave controlled through special electronic circuitry (CRI, Cambridge, MA). Liquid crystal retarders were calibrated using an optical bench set-up, including a monochromatic light source, high extinction polarizers and a Babinet Soleil compensator. The liquid crystals in the microscope set-up are controlled by a desk top computer (Quadra 800, Apple Computer, Cupertino, CA) used for instrument control and image processing. A scientific grade video camera (CCD C72, Dage-MTI, Michigan City, IN) records images of specimens illuminated under different polarization conditions (Fig. 2). A frame grabber board (LG-3, Scion Corp., Frederick, MD) in the computer digitizes the video signal (640 \times 480 pixels, 8 bit per pixel) and stores up to 128 individual frames captured at video rate (30 frames per second). In addition to digitizing the video signal, the LG-3 frame grabber board also provides the control voltages for the liquid crystal devices, with the capability of synchronizing frame capture with changes in liquid crystal settings. The software for instrument control and image processing is based on NIH Image, a public domain program by Wayne Rasband (National Institutes of Health, Bethesda, MD; NIH Image is available by anonymous ftp from zippy.nimh.nih.gov/pub/nih-image). We wrote specialized NIH Image macros, procedures and source code to semi-automate the task of image capture, retarder control, data processing, computation and display.

Before being digitized, images are analog enhanced in the camera controller box using the camera gain and black level controls. Manual controls are first set without a birefringent specimen in the optical path (typically, the specimen, sandwiched between slide and coverglass, is moved sideways until a clear region is imaged). The camera black level is adjusted with the extinction setting ($A = \lambda/4$ and $B = \lambda/2$) to render the background image nearly black. Then the camera gain is adjusted to make image intensities with any of the other three retarder settings read a medium grey (typically 150 out of 255 intensity values). With the camera controls set, the liquid crystal control voltages are now fine adjusted so as to give the lowest intensity for the extinction setting and an equal, medium grey intensity for all three other settings (see Eqs. 4a–4d). This procedure of adjusting the retarder voltages to read equal image intensities for settings given

by Eqs. (4b), (4c) and (4d) ensures that the retardance increment X is the same for all three settings (X is typically 16 nm, see Fig. 2).

After all the necessary adjustments are completed, a stack of background images at the four retarder settings are captured. To reduce noise typically 8 to 32 frames are recorded for each retarder setting and frame averaged. The stack of four, frame averaged images, one for each retarder setting, is then used to compute two images representing the α_{minBG} and β_{minBG} background values in each pixel (see section on background correction procedure). Then the specimen of interest is moved into the viewing field and another stack of four images is recorded (see Fig. 2). With these four images the specimen retardance is computed (see Fig. 3). For best results the background correction procedure discussed earlier is applied during the calculation.

With the instrumentation and procedures described above we achieved a noise level corresponding to 0.1 nm root mean square retardance with single frame capture of the specimen stack (no frame averaging). The noise level is a direct measure of the sensitivity of the instrument. Specimen retardances smaller than the noise level remain undetected, while specimen retardances larger than the noise floor clearly stand out in the image. With single frame capture, the elapsed time between the first frame captured with the first retarder setting and the fourth frame captured with the fourth retarder setting is 0.43 s or 13 video-frame times: one frame for each capture and three frames waiting time for each change of the liquid crystal retarder settings (the liquid crystal devices in use settle to a new retardance value in just under 100 ms or three frame times). With a static or nearly static specimen, several video frames can be averaged for each retarder setting, resulting in a reduction of camera noise and an increase in sensitivity. With slowly moving specimens, frame averaging can increase sensitivity at the expense of time and spatial resolution.

6. Conclusions

The new instrument dramatically enhances the unique capabilities of the traditional polarized light microscope to measure submicroscopic molecular order. It can do so independent of specimen orientation at high spatial and temporal resolution, concurrently for the whole field of view. These significant advances will launch new investigations into the structure and dynamics of molecular organization in application areas that traditionally harness the analytical power of the polarized light microscope.

Acknowledgments

We gratefully acknowledge the inspiration and support

provided by Shinya Inoué. We thank our collaborators Robert E. Palazzo, University of Kansas, Edward D. Salmon and Phong T. Tran, University of North Carolina, for helpful discussions and for generously providing samples. We wish to thank Robert A. Knudson for assisting in the design and fabrication of mechano-optical parts. We also thank Nikon Corporation for instrument support. The instrument development is supported by the National Institutes of Health grants R01 GM49210 awarded to R.O. and R37 GM31617 awarded to S.I.

References

- Allen, R.D., Brault, J. & Moore, R.D. (1963) A new method of polarization microscopic analysis I. Scanning with a birefringence detection system. *J. Cell Biol.* 18, 223–235.
- Chamot, E.M. & Mason, C.W. (1958) *Handbook of Chemical Microscopy*, 2nd edn. John Wiley & Sons, New York.
- Chipman, R.A. (1989) Polarization analysis of optical systems. *Opt. Eng.* 28, 90–99.
- Hansen, E.W., Conchello, J.A. & Allen, R.D. (1988) Restoring image quality in the polarizing microscope: analysis of the Allen video-enhanced contrast method. *J. Opt. Soc. Am.* 5, 1836–1847.
- Hartshorne, N.H. & Stuart, A. (1960) *Crystals and the Polarising Microscope: A Handbook for Chemists and Others*, 3rd edn. Arnold, London.
- Inoué, S. (1986) *Video Microscopy*. Plenum Press, New York.
- Inoué, S. & Hyde, W.L. (1957) Studies on depolarization of light at microscope lens surfaces II. The simultaneous realization of high resolution and high sensitivity with the polarizing microscope. *J. Biophys. Biochem. Cytol.* 3, 831–838.
- Inoué, S. & Kubota, H. (1958) Diffraction anomaly in polarizing microscopes. *Nature*, 182, 1725–1726.
- Inoué, S. & Sato, H. (1966) Deoxyribonucleic acid arrangement in living sperm. *Molecular Architecture in Cell Physiology* (ed. by T. Hayashi and A. G. Szent-Gyorgi), pp. 209–298. Prentice-Hall, Englewood Cliffs, NJ.
- Kliger, D.S., Lewis, J.W. & Randall, C.E. (1990) *Polarized Light in Optics and Spectroscopy*. Academic Press, New York.
- McCrone, W.C. (1991) Light microscopy. *Physical Methods of Chemistry* (ed. by B. W. Rossiter and J. F. Hamilton), pp. 343–443. John Wiley & Sons, Inc.
- Mei, G. & Oldenbourg, R. (1994) Fast imaging polarimetry with precision universal compensator. *Proceedings of the Polarization Analysis and Measurement II*, pp. 29–39. SPIE—The International Society for Optical Engineering.
- Oldenbourg, R., Mei, G. & Palazzo, R.E. (1993) Asters in lysates of *Spisula* oocytes observed with a new type of polarized light microscope. *Biol. Bull.* 185, 288.
- Shurcliff, W.A. (1962) *Polarized Light, Production and Use*. Harvard University Press, Cambridge, MA.
- Tran, P.T., Inoué, S., Salmon, E.D. & Oldenbourg, R. (1994) Muscle fine structure and microtubule birefringence measured with a new pol-scope. *Biol. Bull.* 187, 244–245.